Multiple populations of extrasolar gas giants

Shohei Goda[1] and Taro Matsuo[1]

[1]Department of Earth and Space Science, Graduate School of Science, Osaka University, 1-1, Machikaneyamacho, Toyonaka, Osaka 560-0043, Japan

ABSTRACT

Statistically verifying the character of exoplanets, we can expect to reveal the formation or evolution processes of planetary systems. The notable parameters of planetary systems are metallicity of host star, planet mass, and eccentricity. Gas giants around metal rich stars are easily formed by core accretion. Since these planets are grown with bottom up, the distributions of planet masses and eccentricities are seemed to be continuously extended. On the other hand, the planetary formation by disk instability depends on mass and effective temperature of protoplanetary disk, but there is no strongly dependence on metallicity of host star. As these planets are not formed with bottom up, the planetary masses and eccentricities ununiformly distribute. In this study, we statistically revealed the planetary distributions of metal-rich and -poor regions, and tried to understand the planetary-formation and -evolution processes. Note that we made the dataset included the both selection biases of planetary detection for metal-rich and -poor regions to ignore the effect of these biases. As the results from classification for those samples with Gaussian Mixture Model, we found that the planetary distribution was divided into 3 regions by the boundaries around 3 and 13 M_J. We also discovered the different distributions of planet mass between each metallicity region, which explains the different processes of the planetary formation: core accretion model is applied in metal-rich region, and several formation models including core accretion are match in metal-poor region. In addition, we found that the distributions of planetary eccentricity have a difference between each mass cluster, especially in metal-rich region, which implies that there are dynamical interactions after the planets formed by core accretion.

Keywords: methods: data analysis – planets and satellites: terrestrial planets

1. INTRODUCTION

Decades ago, the discussion of planetary formation in solar system was developed for the solar system (Hayashi et al. 1985). Two representative formation scenarios for Jupiter have been proposed: Core accretion (Perri & Cameron 1974; Mizuno 1980; Pollack et al. 1996) and disk instability (Kuiper 1951; Boss 1997; Mayer et al. 2002). In theory, the two planetary-formation processes have different dependences on disk metallicity, which is defined as the ratio of the metal-number-density to hydrogen atoms, and planet mass (e.g., Matsuo et al. 2007).

For the core accretion model, a proto-planet core easily grows to the critical core mass before the disk gas dissipates. This occurs because the disk metallicity reflects the building materials available for the core (Ida & Lin 2004b; Mordasini et al. 2012). In fact, since the first planet orbiting a normal star was discovered (Mayor & Queloz 1995), large-sized radial velocity observations have revealed that, while the metallicities of stars hosting smaller planets such as Neptune-like planets and super-Earths are significantly lower than those of stars orbited by extrasolar gas giants (Mayor et al. 2011; Wang & Fischer 2015), the gas giants preferentially orbit metal-rich stars (e.g., Santos et al. 2003; Fischer & Valenti 2005). Because the central star and its surrounding protoplanetary disks are formed from a same molecular cloud, according to the primordial hypothesis, most gas giants are thought to have formed via the core accretion. Regarding the planet mass, the gas giants with planet mass up to 30 M_J are potentially formed via the core accretion (e.g., Tanigawa & Ikoma 2007; Tanigawa & Tanaka 2016). The number of the gas giants also de-

creases as the planet mass is higher (e.g., Mordasini et al. 2009).

For the disk instability scenario, there are various reports about the relationship between disk metallicity and disk-instability-induced planetary formation; there exists reports of negative correlation (Cai et al. 2006; Durisen et al. 2007), a very weak positive correlation (Mayer et al. 2007), and no correlation (Boss 2002) in the metallicity range of the stars hosting the observed planets. Although the lower limit on the masses of the disk-instability-induced planets may exist (Matsuo et al. 2007), the mass distribution of the gas giants formed via the disk instability still remains an open question. On the other hand, direct imaging of extrasolar planets orbiting HR8799, Formalhaut, and beta Pictoris reported in 2008 and 2010 (Marois et al. 2008; Kalas et al. 2008; Lagrange et al. 2010), respectively, confirmed the existing of outer planets, which can be naturally explained by the disk instability scenario rather than the extended core accretion with migration or planet-planet scattering (Dodson-Robinson et al. 2009). Thus, there may exist two populations originated from the two planetary formations.

Several previous studies showed that the gas giants are divided into two regimes with a boundary mass of 4 M_J and interpreted the two populations as an outcome originated from the two planetary formations (Ribas & Miralda-Escudé 2007; Santos et al. 2017; Schlaufman 2018); while the gas giants lighter than 4 M_J are core-accreted planets, the gas giants more massive than 4 M_J may be formed through disk instability. However, it is possible to form very massive gas giants up to 30 M_J via the core accretion in theory (e.g., Tanigawa & Tanaka 2016)(e.g., Tanigawa et al. 2008; Mordasini et al. 2009; Tanigawa & Tanaka 2016) and the upper mass limit of the core-accreted planets is also expected to depend on the disk metallicity (Mordasini et al. 2012). Pebble accretion has been recently proposed as the third planetary formation scenario that enables massive core to be formed in the outer region beyond 10 au (Ormel & Klahr 2010; Lambrechts & Johansen 2012); more massive planets than the core-accreted planets are potentially formed thanks to wider hill radius. Thus, whether the boundary mass of 4 M_J can be applied as the upper boundaries of the bottom-up planetary formation scenarios such as the core accretion and pebble accretion is still unknown. Furthermore, although the previous studies did not consider the selection effects of the planet detections, the detection limits of the radial velocity measurements clearly depend on the metallicity of the host star (see Figure 1, (a)).

In this paper, we re-investigate what the upper-mass limits of the bottom-up planetary formation scenarios are and explore the possibilities of multiple populations in the extrasolar planetary systems discovered to data through evaluating the distributions of the planet masses and eccentricities in the metal-rich and -poor regions, minimizing the measurement biases for the host-star metallicity and stellar mass, which are not derived by using the uniform method (e.g., Santos et al. 2004; Sousa et al. 2008), and the detection biases of the radial velocity measurements. This paper is organized as follows. In Section 2, we explain how the samples gathered for this study were composed and how the distributions of the planet masses, eccentricities, and semi-major axes in the metal-rich and -poor regions were evaluated. In Section 3, we derive the boundary metallicity that is divided into two regions such that the distributions of the planet masses and semi-major axes are most different and investigate how the samples are divided with the Gaussian mixture model. In Section 4, we discuss what the upper-mass limit of the gas giants formed via the bottom-up planetary formation is and whether the disk-instability-induced planetary formation occurs.

2. METHOD

In this section, we explain how to perform statistical analysis for extrasolar gaseous objects to understand their formation and evolution process and show how to deal with the selection effect of radial velocity measurements by which samples constructed for this study were detected. We also explain how we constructed the samples used in this study, determining the boundary between gas dwarfs such as Neptune-like planets and gaseous giants.

2.1. *Statistical Analysis*

In this study, we first examined whether the distributions of semi-major axes and planet masses for gaseous objects arise from the selection effect of radial velocity measurements or from the dependency of the planetary formation and evolution process on the disk metallicity, constructing samples named as "common-biased samples" that minimize an impact of the selection effect on the distributions, as to be discussed in Section 2.2. Given that the measurement errors follow a normal distribution, we sampled the host star metallicities and companion masses and divided the common-biased samples into two by a host-star metallicity. Using the "anderson_ksamp" module in Python, we compared the divided sub-samples in terms of planet mass and semi-major axis with two-sample Anderson-Darling test. Calculating the p-values derived from the two-sample Anderson-Darling test as a function of the host

star metallicity, we searched for a boundary metallicity that divides the common-biased samples such that the distributions of companion masses and semi-major axes for the two sub-samples are most different. We iterated this procedure 1,000 times and finally evaluated how much different the two common-biased sub-samples are in terms of the semi-major axis and planet mass at the boundary metallicity. This result is shown in Section 3.1.

Next, we explored how many populations exist in extrasolar gaseous objects discovered so far to investigate what the upper mass limit of the core-accreted planets is; we re-examined whether only two populations exist in the extrasolar gaseous objects, as shown in several previous studies (Ribas & Miralda-Escudé 2007; Santos et al. 2017; Schlaufman 2018). Using the "GaussianMixture" package in Python, we applied two-dimensional Gaussian mixture model to the diagram of host star metallicities versus companion masses and for the common-biased samples. The number of the Gaussian mixture models used for this cluster analysis ranges from 1 to 10. We determined the number of the components of the best Gaussian mixture model based on the Bayesian Information Criterion as well as to which each common-biased sample belong. Sampling the host star metallicities and companion masses, we repeated this procedure 1,000 times. This result is introduced in Section 3.2.

2.2. *Common-biased Samples*

In order to reveal the distributions of companion mass and orbital properties for companions orbiting various host-star metallicities, we gathered extrasolar gaseous objects discovered by radial velocity observations that precisely determine lower limit of companion mass, semi-major axis and eccentricity. The gathered objects are referred to as "original samples" in this paper. Considering that there may exist the relation between the planetary-formation processes and the host-star metallicity, as discussed in Section 1, it is preferable that the accuracies and terms of the radial velocity measurements, which detected the original samples, are independent of the host-star metallicity. This is because the original samples detected via radial velocity measurements are influenced by two selection effects: (i) limited sensitivity to long-period planets owing to short observation terms and (ii) limited sensitivity to low-mass planets owing to a lack of measurement precision in radial velocity measurement. The semi-major axis, $a|_{max}$, and lower mass limit, $Mp \sin i|_{min}$, of the detectable companion can be determined by the accuracy, σ, and term, τ, of the radial velocity measurements as below

(Torres et al. 2008),

$$a|_{max} = M_*^{\frac{1}{3}} \tau^{\frac{2}{3}}, \tag{1}$$

$$M_p \sin i|_{min} \approx 4.919 \times 10^{-3} P^{\frac{1}{3}} (1 - e^2)^{\frac{1}{2}} M_*^{\frac{2}{3}} \sigma, \tag{2}$$

where, M_*, P, and e are the stellar mass, the orbital period and eccentricity of the companion, respectively. The region in which a companion can be detected is derived for each radial velocity measurement based on Equation (1) and (2). Figure 1, (a) compares the detectable probabilities of a companion with radial velocity measurements in a diagram of period versus lower limit of companion mass for the metal-rich and -poor regions. Note that the boundary metallicity was fixed to 0 dex. As shown in Figure 1, the accuracies of the radial velocity observations for the metal-poor original samples are clearly worse than those for the metal-rich ones. In contrast, the detectable semi-major axis for the original samples orbiting the metal-rich stars are slightly wider compared to those of the metal-poor samples. Thus, the selection effect of the radial velocity measurements depends on the host-star metallicity and affect the distributions of masses and semi-major axes for the two original sub-samples orbiting the metal-rich and -poor samples.

Focusing on a fact that the distributions of masses and semi-major axes for the original samples discovered in the metal-rich (-poor) region are biased with the selection effect of the radial velocity measurements for the metal-rich (-poor) stars, we can minimize the impact of the different selection effects on the original samples through filtering the metal-rich (-poor) original samples with the selection effect in the metal-poor (-rich); the selection biases in the metal-rich and -poor stars were equalized (see Figure 1, (b)). The filtering process judges whether each original sample simply satisfy the following criteria:

$$M_p \sin i - M_p \sin i|_{min} \geqq \frac{1}{2}(a - a|_{max}), \tag{3}$$

$$a \leqq a|_{max}. \tag{4}$$

Now, we refer the filtered samples to as "common-biased samples."

2.3. *Preparation of Samples*

The original samples considered in this study are limited to companion objects detected by the radial velocity observations, allowing the orbital parameters to be characterized and lower limit of the companion mass to be determined. Essentially, the original samples are selected from those labeled "Radial Velocity" in the "detection method" column of the Extrasolar Planet Encyclopedia catalog as of the end of June 2018 (Schneider
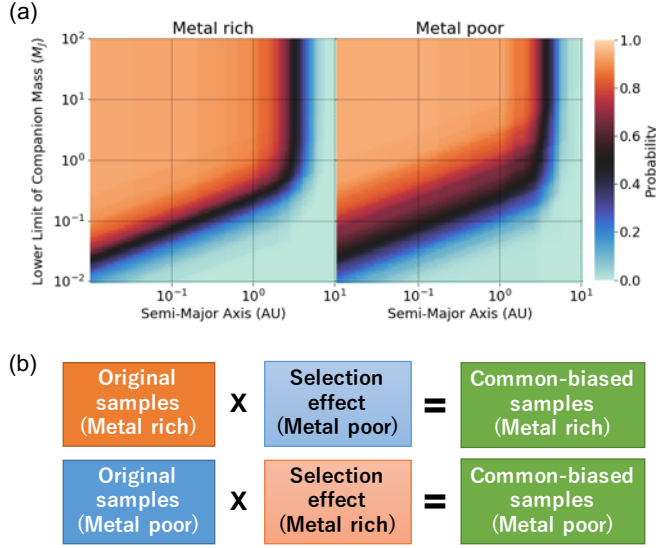
Figure 1. (a) Detection probabilities of a companion in a diagram of semi-major axis versus companion mass with the radial velocity measurements for the metal-rich (left) and -poor original samples (right) divided by a metallicity of 0 dex. The probability was defined as the fraction of the number of the radial velocity measurements that can detect a companion to the total of the measurements in each metallicity region. (b) Procedure for equalizing the selection biases included in the original samples in two different metallicity regions. The original metal-rich (-poor) samples were additionally filtered with the selection effects constructed from the radial velocity measurements of the metal-poor (-rich) samples. The filtered original samples were defined as "common-biased samples" that are biased by a common selection effect. The filtering procedure judges whether the original samples can be detected by radial velocity measurements with the constructed selection effect, and the filtered samples are included in the common-biased samples only when the original samples are detectable.

et al. 2011). The radial velocities of the host stars orbited by the original samples, and the orbital periods and eccentricities of the original samples are also collected from the same catalog. The SWEET-Cat catalog was referred to for the metallicity and mass of the host star (Santos et al. 2013; Sousa et al. 2018); this catalog presents the uniformly derived stellar parameters of the planet host stars. For some of the original samples that are not listed in the SWEET-Cat catalog, the metallicities and masses measured by the Geneva-Copenhagen catalog (Casagrande et al. 2011) the Padova database (Girardi et al. 2000), and the BaSTI stellar model (Hidalgo et al. 2018) were applied and were calibrated by using regression lines determined from the correlations between the values in the SWEET-Cat catalog and those in the three catalogs to minimize measurement biases

for host-star metallicities and masses. Using the stellar mass and the lower limit of companion mass was newly calculated based on Equation 2 because the host-star masses were revised.

The measurement accuracy and observation term for the radial velocity measurement of each original sample as the indicators of the selection effect were extracted from the exoplanets.org catalog. According to the Kepler's third law shown in Equation 1, the observation term and stellar mass provide the upper limit on the semi-major axis of a detectable companion with the radial velocity measurement of each original sample. Using the derived maximum semi-major axis, host-star mass and measurement accuracy, the lower limit on the mass of the detectable companion was derived based on Equation 2.

2.4. Boundary between Gas Giants and Neptune-like Planets

The gaseous objects were extracted from all the samples in the Extrasolar Planet Encyclopedia catalog in order to remove the impact of low-mass samples, such as Neptune-mass planets (gas dwarfs) and super-Earths, on this analysis. First, we determined the boundary mass between the gaseous and gas-dwarf objects from a perspective of both theory and observation. According to a previous study (Ida & Lin 2004a), gas-dwarf objects, which primarily consist of heavy-core objects such as Neptune and Uranus, have the potential to grow to the extent allowed by the core building materials inside their semi-major axes. This growth occurs via giant impacts in the inner region of the disk after the disk gas dissipates. However, this core growth is limited by the scattering effect of the heavy core increasing with greater distances from the central star. Therefore, the mass of a gas-dwarf object reaches a maximum at the semi-major axis, where the scattering effect begins to limit the core growth. Given that the ratio of collision-to-ejection probabilities for the heavy core is 0.1 and the core density is 1 g/cm^3, the upper mass limit of the gas-dwarf object is approximately 0.1 M_J for dust surface densities of 3 times the Minimum Solar Nebulae Model value (MMSN).

From a standpoint of the observation, a boundary between gas giants and gas dwarfs at four times the Earth's radius has been observationally revealed by the Kepler data (Buchhave et al. 2012). From the empirical planetary mass-radius relation (e.g., Bashi et al. 2017):

$$\frac{R_p}{R_\oplus} \propto \frac{M_p}{M_\oplus} \pm 0.02, \tag{5}$$

we found that the boundary of planetary mass is about 30 times the Earth's mass, corresponding to 0.1 M_J.

Thus, 0.1 M$_J$ was applied in this study as the boundary mass between gas giants and gas dwarfs. The numbers of samples and their planetary systems considered in this study are 623 and 520, respectively.

3. RESULTS

In this section, we quantitively show how different the distributions of the orbital properties and planet masses for the extrasolar gaseous objects orbiting the metal-rich and -poor regions are, minimizing the impact of the selection effect on their distributions. We also explore how many components exit in the extrasolar gaseous objects through classifying the common-biased samples with the Gaussian mixture model.

3.1. *Two Metallicity Regions*

We first determined the boundary of metallicity that divides the original samples into two such that the distributions of planet mass and semi-major axis in the two metal-rich and -poor regions are most different, respectively, using the method that considers the selection effects of the radial velocity measurements, as explained in Section 2.1. Figure 2 shows the p-values derived by the two-sample Anderson-Darling test for the distributions of the semi-major axes and lower mass limits of the common-biased samples, changing the boundary of metallicity from -0.7 to 0.4 dex. Note that the common-biased samples, which were applied to the two-sample Anderson-Darling test, were constructed such that the impacts of the selection effects in the metal-rich and -poor regions on the common-biased sub-samples are equalized; the comparison between the two distributions of the common-biased sub-samples is not affected by the selection effects of the radial velocity measurements. We iterated the calculation 1,000 times and averaged the calculated p-values for each divided point to derive the mean and standard deviation of the p-values. The minimum p-values of the two-sample Anderson-Darling tests for the distributions of the semi-major axis and the planet mass were 2.4×10^{-3} and $3.5 \times 10^{-5}/4.2 \times 10^{-5}$ at the metallicity of -0.04 and -0.29/-0.06 dex, respectively; thus, the planetary distributions in the metal-rich and -poor regions do not arise from the selection effect of the radial velocity measurements but from the planet formation and evolution. In this study, we used applied -0.05 dex as the boundary of metallicity through considering that the two minimum p-values are around -0.05 dex.

Next, we compared the distributions of the lower mass limit and semi-major axis for the common-biased sub-samples in the metal-rich and -poor regions that are divided by the boundary of metallicity. Figure 3 shows
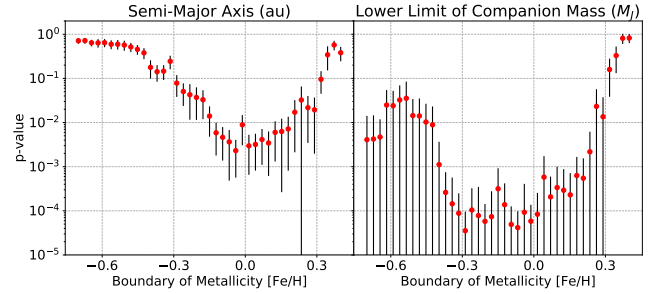

Figure 2. P-values calculated via two-sample Anderson-Darling tests for the semi-major axis (left) and the lower limit of the companion mass (right) of the original samples as a function of the boundary of metallicity. The red points and black vertical bars represent the mean p-values and their standard deviations, respectively. The number of the calculations for each boundary of metallicity is 1,000.

two scatter plots of the common-biased sub-samples in the metal-rich and -poor regions on the semi-major axis and lower-mass limit and compared the cumulative fractions of the common-biased sub-samples in terms of the semi-major axis and lower-mass limit, respectively. The gas giants with semi-major axis less than 0.1 au and the planets more massive than about 5 M$_J$ in the metal-poor region are relatively lack and excess compared to those in the metal-rich region, respectively. We discuss where the difference between the planetary distributions in the metal-rich and -poor regions comes from in Section 4.

3.2. *Three Mass-Regimes of Gaseous Objects*

We classified the 623 common-biased samples into multiple sub-samples on the host-star metallicity and planet-mass plane with the Gaussian mixture model to explore how many sub-samples exist in the extrasolar gas giants discovered to data, given that each sub-sample follow a normal distribution (e.g., Santos et al. 2017; Schlaufman 2018). Changing the number of the sub-samples, we evaluated each model with the Bayesian Information Criterion and found that the three-component model is suitable as the best Gaussian mixture model for the 623 common-biased samples. Figure 4 shows the best suited model for the common-biased samples. The common-biased samples are divided into three almost along two boundary masses of 4 and 20 M$_J$. The three-component model results from relative paucity of the common-biased samples in two specific regions in the diagram of host-star metallicity versus companion mass; the two regions indicate gaseous objects with masses ranging from 20 to 30 M$_J$ around both the metal-rich and -poor stars and those with masses ranging from 0.1 to 4 M$_J$ around the metal-poor stars. The mean metallicity of the stars hosting the gaseous objects
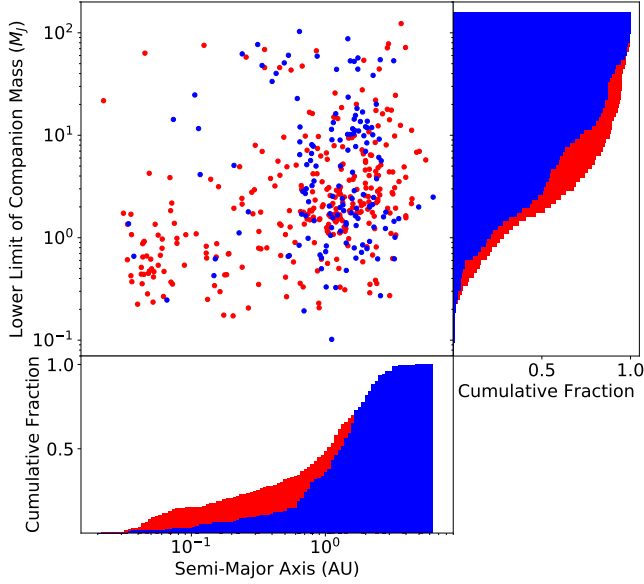
Figure 3. Distribution of the semi-major axes and lower limits of companion mass for the common-biased samples (upper left) and the cumulative distributions of semi-major axis (bottom) and lower limit of companion mass (right). The red and blue points/bins represent the metal-rich and -poor samples, respectively. An example among the 1,000 calculations was shown.

Figure 4. Distribution of the host-star metallicity and lower limit of companion masses for three common-biased sub-samples classified by the Gaussian mixture model. The different symbols of square, triangle, and circle represent the classified sub-samples. The blue, green, and red colors are three-mass regimes with two boundary masses of 4 and 20 M_J shown by the horizontal long-dashed lines. The vertical short dashed lines and gray regions in the three-mass regimes show the mean metallicity and its standard error in each regime, respectively. An example among the 1,000 calculations was shown.

more with masses from 4 to 20 M_J is lower than that of the lighter samples and the mean metallicity of the samples more massive than 20 M_J is much lower than those of the other two sub-samples. Thus, the three-mass regimes exist in the extrasolar gaseous objects discovered so far instead of the two-mass regimes proposed by the previous studies (Ribas & Miralda-Escudé 2007; Santos et al. 2017; Schlaufman 2018). Based on the theoretical studies on the maximum mass of the core-accreted planet (e.g., Mordasini et al. 2012; Tanigawa & Tanaka 2016), we redefined the samples lighter than 20 M_J as planetary-mass objects and labeled the two sub-samples with masses from 0.1 to 4 M_J and from 4 to 20 M_J as "intermediate-mass planets" and "massive planets." In addition, the samples more massive than 20 M_J are labeled as "brown dwarfs." Note that the boundary between planetary mass and brown dwarf objects established by the deuterium-burning minimum mass of 10 M_J mentioned in a previous study is semantic (Chabrier et al. 2014); this boundary has no physical meaning from the perspective object evolution.

We next investigated the eccentricity distributions of the brown dwarfs, massive planets, and intermediate-mass planets in both the metal-rich and -poor regions, respectively. The upper panels of Figure 5 are scat-
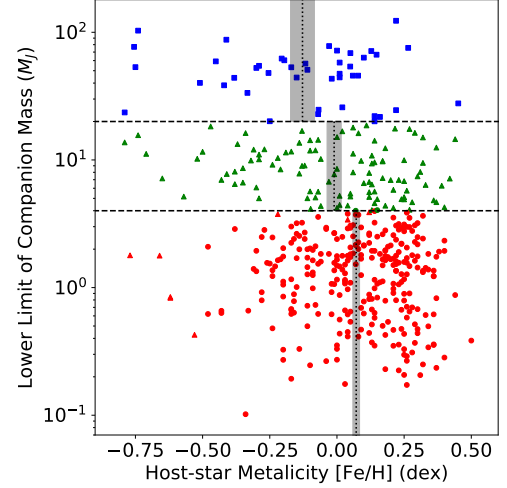
ter plots of the common-biased samples in the diagram of eccentricity versus companion mass in the metal-rich and -poor regions. The bottom panels are the cumulative fractions of the eccentricities for the three populations orbiting the metal-rich and -poor stars, respectively. The observational result common to the common-biased samples orbiting the metal-rich and -poor stars is that, while the eccentricities of the brown dwarfs uniformly distribute from 0 to 1, about 80 % of the intermediate-mass planets have eccentricities smaller than 0.3. In contrast, the eccentricity distributions of the massive planets in the metal-rich and -poor regions are largely different; while the cumulative fraction of the eccentricities for the massive planets orbiting the metal-rich stars is close to that of the brown dwarf, that of the metal-poor massive planets is consistent with that of the intermediate-mass planets. In fact, as shown in Figure 6, the mean eccentricity of the massive planets decreases as the metallicity of the host star decreases. Thus, the eccentricity distributions also support the three-mass regimes of the extrasolar gaseous objects.
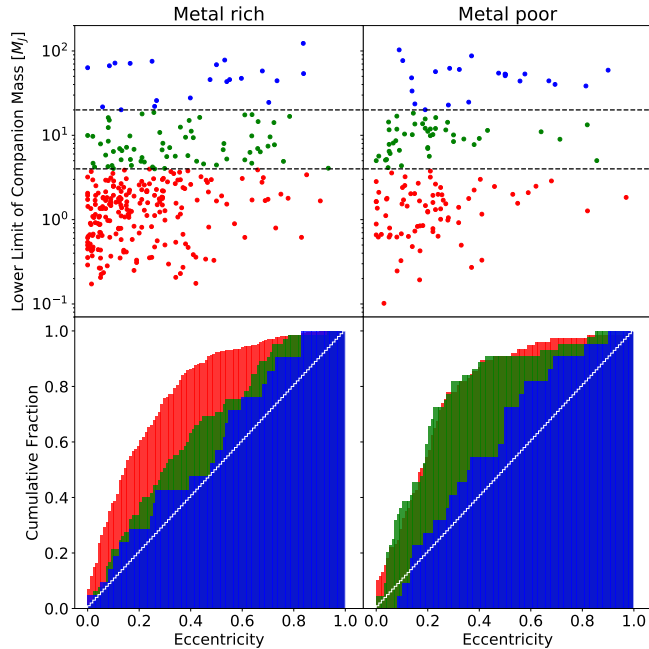
4. DISCUSSION

Figure 5. Distributions of eccentricities and lower limits of companion mass (top) and the cumulative distributions of eccentricities for the common-biased samples orbiting the metal-rich and -poor regions (bottom). The horizontal lines and three colors represent same as those of Figure 4. The white line is the cumulative uniform distribution.
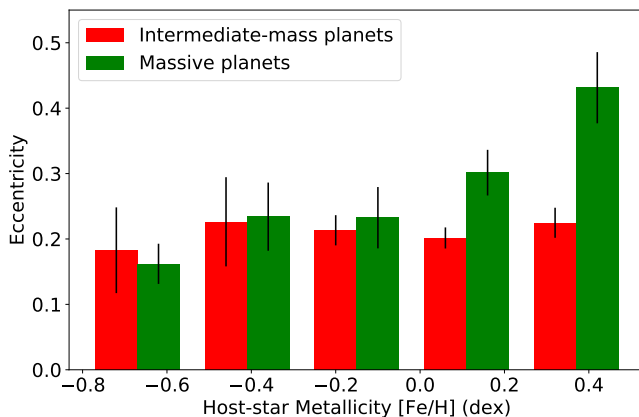

Figure 6. Histograms of eccentricities for the common-biased intermediate-mass planets (red) and massive ones (green) as a function of the host-star metallicity. The width of each bin was set to 0.26 dex. The height and vertical bar of each bin represent the mean eccentricity and its standard error for the common-biased intermediate-mass and massive planets belonging to each range.

In this section, we compare the above results of planetary mass and eccentricity distributions with previous

studies and verify the relationship. We also discuss the behavior of planetary distributions in the metal-rich and -poor regions, comparing the observed dataset from the simulation of Mordasini et al. (2012).

4.1. Core Accretion Model

In Mordasini et al. (2012), planets are formed by classical core accretion model, and the final semi-major axes and planetary masses are determined, based on the simulation included the planetary migration in disks and the disk evolution. From our study, the two observed planetary-mass distributions, which were divided by the metal boundary, had different expanses. Then, we discuss each planetary-formation process, comparing the distribution of observed data with that of simulation data. Figure 7 shows that the comparison between the observed data included the selection biases and simulation data cited from Mordasini et al. (2012). The simulation data were also filtered by both selection biases of metal-rich and -poor regions to complete the conditions with the observed data. As the result, the distributions of metal rich regions are very consistence, which can explain that most of gas giants in the metal rich region are formed by core accretion. This is also explained by our results shown in Section ?? because of below interpretation. The interaction between a gas giant and protoplanetary disk possibly makes the eccentricity of planet grow (e.g., Goldreich & Sari 2003; Kley & Dirksen 2006). This interaction is concentrated at discrete Lindblad and corotation resonances, which causes the planet's orbit to migrate and open a gap in the disk as the planet mass is large enough. If the viscous coefficient equals to 10^{-5} , the planet with circular orbit changes to eccentric orbit as the planetary mass is over 3 M_J . The more massive planets make their eccentricity higher until the maximum value 0.25. On the other hand, if a planetary system has two gas giants, the outer planet may prolong the orbital period of the inner planet. These planets' eccentricities grow up in rough inverse proportion to their masses by this orbital interaction (Chiang et al. 2002). From the verification of simulation (Ida et al. 2013), gas giants and rocky/icy planets emerge, migrate, and undergo dynamical instability in a relatively massive disk, and the perturbation between planets causes orbital crossing, eccentricity excitation, and planetary ejection. Therefore, gas giants formed through core accretion tend to have high eccentricities, which is consistent to our results of eccentricity distribution.

In contrast, the distributions of metal poor regions between the observed data and the simulation data are different. This means that the planetary formation pro-

cess in metal poor disks differs from in metal rich disks: the planetary formation in metal poor region cannot be explained by only core accretion. On the other hand, the eccentricity of gas giant formed via disk instability ranges from 0 to 0.35 in initial stage, and decreases as the planet mass increases (Boss 2011). Note that the range of semi-major axis is 30 to 70 AU. This trend can be also seen slightly in the metal poor region of Figure 5. However, because it is not clear, there possibly exists other formation processes included core accretion in metal poor regions.

According to the previous studies (e.g., Ribas & Miralda-Escudé 2007; Santos et al. 2017; Schlaufman 2018), extrasolar gaseous objects are simply divided into two with a boundary mass of 4 M_J and/or a transition of 4 to 10 M_J; while the gas giants lighter than 4 or 10 M_J are likely to be formed via the core accretion process, disk-instability-induced planetary formation occurs beyond 10 M_J. However, as discussed above, the upper mass limit of the core-accreted planets which is consistent with the theoretical expectations (e.g., Tanigawa & Ikoma 2007; Mordasini et al. 2012; Tanigawa & Tanaka 2016).

4.2. *Beyond the Core Accretion Model*

The excess of massive planets orbiting metal-poor stars differs from that expected form the core accretion formation theory in terms of the following two points. While more massive planets are likely to be formed around more metal-rich stars (Mordasini et al. 2012), the mean masses for the intermediate-mass and massive planets clearly increases as the metallicity decreases (Figure 7). In addition, although a continuous decrease in the mass function of massive planets is theoretically predicted (Mordasini et al. 2009), the observation samples orbiting the metal-poor stars are clustered around 1 and 10 M_J (Figure 3). The eccentricities of the massive planets orbiting metal-poor stars also differ from those around metal-rich stars (Figure 6); the eccentricities of the massive planets around the metal-poor stars do not seem to be enhanced through the planet-disk interaction prior to gas dissipation. Thus, the distributions of masses and eccentricities for the massive planets are unlikely in the bottom-up scenarios.

An explanation for the excess massive planets orbiting metal-poor stars is that the disk instability acts in the vicinity of metal-poor stars, because a lower mass limit applies for planets formed via the disk instability mechanism (i.e., corresponding to an order of the Jeans mass (Matsuo et al. 2007) (Mayor 2011?). As a result, a sharp increase appears in the planetary mass function around 4 M_J. It is also accepted that planet forma-
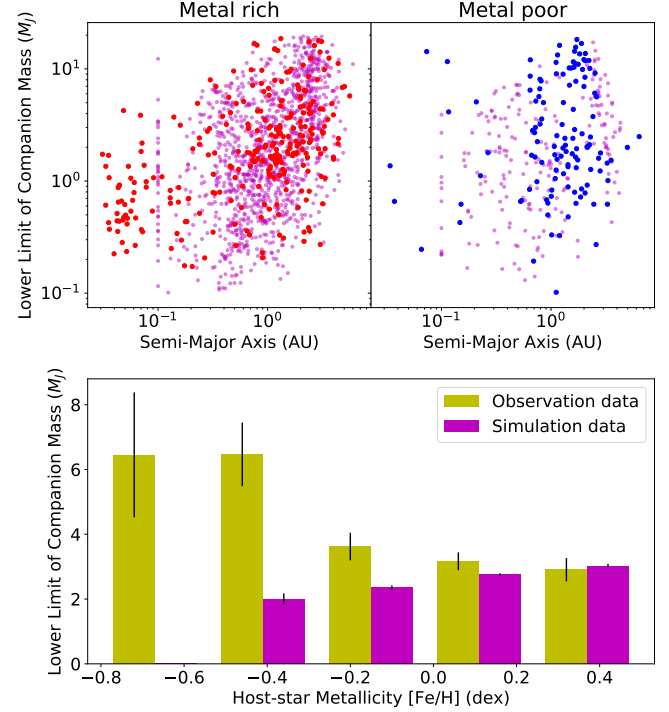

Figure 7. Comparison of planetary distributions between the observed data (red and blue points) and simulation data (yellow and cyan points) in the metal-rich region (upper left) and the metal-poor region (lower left), and the cumulative maps of planetary masses in the metal-rich region (upper right) and the metal-poor region (lower right).

tion due to disk instability tends to occur in the vicinity of metal-poor stars because the cooling timescale in the disk mid-plane is reduced owing to low disk opacity (Cai et al. 2006; Durisen et al. 2007). The low eccentricities of the massive planets orbiting the metal-poor stars are also consistent with the numerical simulations (Mayer 2010?; Mayer et al. 2004?) and the eccentricities of four gas giants orbiting HR8799 (Wertz et al. 2017?). Note that the four gas giants are located in a region beyond the core accretion model.

4.3. *Two Planetary Formation Scenarios*

Based on these considerations, we compared the distribution of host star metallicities and companion masses for the 623 common-biased samples with the regions expected from the core accretion and disk instability models (Figure 8). The scarce regions appear in terms of companion mass, one at 0.1 to 4 M_J and one at 20 to 30 M_J. Whereas the former arises from the rapid gas accretion onto the core, the latter represents a gap between binary star and planet formation. In other words, the two regions reflect the lower and upper mass lim-

its of extrasolar gaseous objects that are formed by the planetary formation processes. In fact, the upper mass limit is almost consistent with the theoretical expectations (Tanigawa & Ikoma 2007; Mordasini et al. 2012; Tanigawa & Tanaka 2016).

While the intermediate-mass and massive planets orbiting the metal-rich stars can be explained by the core accretion model, the excess of massive planets is likely to be explained by the top-down model such as gravitational instability instead of the bottom-up scenario. The previous observational studies on dual planetary formation scenarios (Ribas & Miralda-Escudé 2007; Santos et al. 2017; Schlaufman 2018) showed that there exists a boundary mass of 4 to 10 M_J in the diagram of host star metallicities and masses for gaseous objects and mentioned that the boundary reflects the transition between the two planetary formations; the upper limit of the core-accreted planets is around 4 M_J. However, we found that the boundary of 4 M_J reflects a population that is likely to be formed via disk instability and expected that planets with masses up to 20-30 M_J can be continuously formed by core-accretion around the metal-rich stars.

REFERENCES

Adibekyan, V. Z., Figueira, P., Santos, N. C., et al. 2013, A&A, 560, A51

Bashi, D., Helled, R., Zucker, S., & Mordasini, C. 2017, A&A, 604, A83

Boss, A. P. 1997, Science, 276, 1836

Boss, A. P. 2002, ApJL, 567, L149

Boss, A. P. 2011, ApJ, 731, 74

Buchhave, L. A., Latham, D. W., Johansen, A., et al. 2012, Nature, 486, 375

Cai, K., Durisen, R. H., Michael, S., et al. 2006, ApJL, 636, L149

Casagrande, L., Schönrich, R., Asplund, M., et al. 2011, A&A, 530, A138

Chabrier, G., Johansen, A., Janson, M., & Rafikov, R. 2014, Protostars and Planets VI, 619

Chiang, E. I., Fischer, D., & Thommes, E. 2002, ApJL, 564, L105

Dawson, R. I., & Murray-Clay, R. A. 2013, ApJL, 767, L24

Dodson-Robinson, S. E., Veras, D., Ford, E. B., & Beichman, C. A. 2009, ApJ, 707, 79

Dupuy, T. J., & Liu, M. C. 2011, ApJ, 733, 122

Durisen, R. H., Reipurth, V. Jewitt, Keil, K., et al. 2007, Univ. of Arizona Press, Tucson 951, 607-622

Fischer, D. A., & Valenti, J. 2005, ApJ, 622, 1102

Girardi, L., Bressan, A., Bertelli, G., & Chiosi, C. 2000, A&AS, 141, 371

Goldreich, P., & Sari, R. 2003, ApJ, 585, 1024

Hayashi, C., Nakazawa, K., & Nakagawa, Y. 1985, Protostars and Planets II, 1100

Hidalgo, S. L., Pietrinferni, A., Cassisi, S., et al. 2018, ApJ, 856, 125

Ida, S., & Lin, D. N. C. 2004a, ApJ, 604, 388

Ida, S., & Lin, D. N. C. 2004b, ApJ, 616, 567

Ida, S., Lin, D. N. C., & Nagasawa, M. 2013, ApJ, 775, 42

Kalas, P., Graham, J. R., Chiang, E., et al. 2008, Science, 322, 1345

Kley, W., & Dirksen, G. 2006, A&A, 447, 369

Kuiper, G. P. 1951, Proceedings of the National Academy of Science, 37, 1

Lagrange, A.-M., Bonnefoy, M., Chauvin, G., et al. 2010, Science, 329, 57

Lambrechts, M., & Johansen, A. 2012, A&A, 544, A32

Lee, K. J., Guillemot, L., Yue, Y. L., Kramer, M., & Champion, D. J. 2012, MNRAS, 424, 2832

Ma, B., & Ge, J. 2014, MNRAS, 439, 2781

Marois, C., Macintosh, B., Barman, T., et al. 2008, Science, 322, 1348

Matsuo, T., Shibai, H., Ootsubo, T., & Tamura, M. 2007, ApJ, 662, 1282

Mayor, M., & Queloz, D. 1995, Nature, 378, 355

Mayer, L., Quinn, T., Wadsley, J., & Stadel, J. 2002, Science, 298, 1756

Mayer, L., Lufkin, G., Quinn, T., & Wadsley, J. 2007, ApJL, 661, L77

Mayor, M., Marmier, M., Lovis, C., et al. 2011, arXiv:1109.2497

Mizuno, H. 1980, Progress of Theoretical Physics, 64, 544

Mordasini, C., Alibert, Y., Benz, W., & Naef, D. 2009, A&A, 501, 1161

Mordasini, C., Alibert, Y., Benz, W., Klahr, H., & Henning, T. 2012, A&A, 541, A97

Ormel, C. W., & Klahr, H. H. 2010, A&A, 520, A43

Perri, F., & Cameron, A. G. W. 1974, Icarus, 22, 416

Pollack, J. B., Hubickyj, O., Bodenheimer, P., et al. 1996, Icarus, 124, 62

Ribas, I., & Miralda-Escudé, J. 2007, A&A, 464, 779

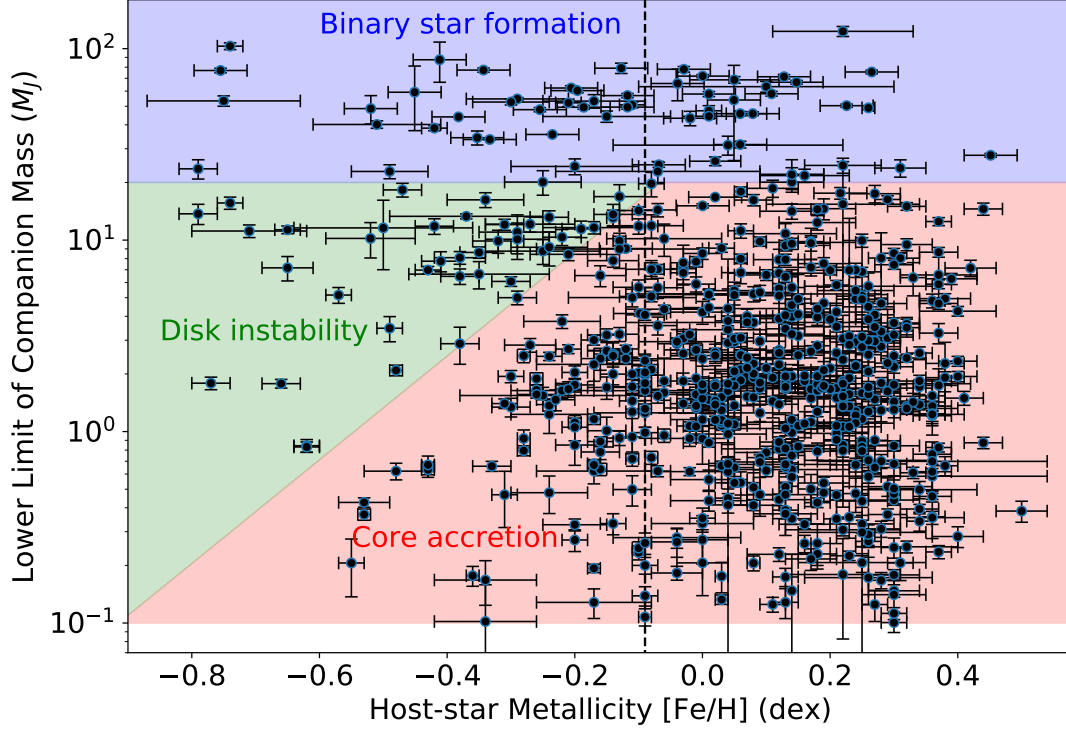Santos, N. C., Israelian, G., Mayor, M., Rebolo, R., & Udry, S. 2003, A&A, 398, 363

Figure 8.

Santos, N. C., Israelian, G., & Mayor, M. 2004, A&A, 415, 1153

Santos, N. C., Sousa, S. G., Mortier, A., et al. 2013, A&A, 556, A150

Santos, N. C., Adibekyan, V., Figueira, P., et al. 2017, A&A, 603, A30

Schlaufman, K. C. 2018, ApJ, 853, 37

Schneider, J., Dedieu, C., Le Sidaner, P., Savalle, R., & Zolotukhin, I. 2011, A&A, 532, A79

Sousa, S. G., Santos, N. C., Mayor, M., et al. 2008, A&A, 487, 373

Sousa, S. G., Adibekyan, V., Delgado-Mena, E., et al. 2018, A&A, 620, A58

Tanigawa, T., & Ikoma, M. 2007, ApJ, 667, 557

Tanigawa, T., & Tanaka, H. 2016, ApJ, 823, 48

Torres, G., Winn, J. N., & Holman, M. J. 2008, ApJ, 677, 1324

Wang, J., & Fischer, D. A. 2015, AJ, 149, 14

APPENDIX

A. UNCONSIDERED FACTORS